Journal of Alloys and Compounds 996 (2024) 174796

Contents lists available at ScienceDirect

Journal of Alloys and Compounds

journal homepage: www.elsevier.com/locate/jalcom

# Enabling high capacity and reversible Li storage in indium(III) oxide anode surrounded by carbon nanotube matrix

Minju Kim [a,1], Chanwoo Park [a,1], Wonjong Jung [b,*], Jaehyun Hur [a,*]

[a] Department of Chemical and Biological Engineering, Gachon University, Seongnam, Gyeonggi 13120, the Republic of Korea
[b] Department of Mechanical, Smart, and Industrial Engineering, Gachon University, Seongnam, Gyeonggi 13120, the Republic of Korea

ARTICLE INFO

*Keywords:*
$In_2O_3$
CNT
Homogeneous mixing
Solvothermal process
Li-ion battery anodes

ABSTRACT

$In_2O_3$ is one of the post-transition metal oxides that can be a potential anode material for the Li-ion batteries (LIBs) because of its high theoretical capacity (869 mAh $g^{-1}$) and low operating voltage (0.8 V vs $Li/Li^+$) compared to other metal oxides. However, they have rarely been used in practical applications because of typical challenges such as irreversible capacity, unstable cycling stability, and poor coulombic efficiency. In this study, carbon nanotubes (CNTs) were successfully combined with $In_2O_3$ nanoparticles (NPs) via a solvothermal process. The $In_2O_3$ NPs and CNTs were homogeneously mixed by controlling the CNT dispersion (functionalization and appropriate solvent) and mixing sequence (dissolving the $In_2O_3$ precursor in the CNT-dispersed solution followed by thermal annealing). In addition, an increase in the oxygen vacancies in the $In_2O_3$ NPs by controlling the thermal annealing conditions ($In_2O_3$/CNT_Ar) could enhance robust binding with CNTs, increase the number of Li-ion binding sites, and improve the electrical conductivity. Therefore, at an appropriate ratio of $In_2O_3$ and CNT (92:8, w/w), the $In_2O_3$/CNT_Ar demonstrated remarkable cycling performance (830 mAh $g^{-1}$ at a current density of 200 mA $g^{-1}$ after 100 cycles) and rate capability (65% retention at 5 A $g^{-1}$ relative to 100 mA $g^{-1}$), which outperformed most $In_2O_3$-based anodes previously studied. Therefore, $In_2O_3$/CNT_Ar is a promising anode material for use in next-generation LIBs.

## 1. Introduction

With the advent of global warming and climate crises, it has become essential to seek green energy sources that can replace conventional fossil energy [1–3]. Lithium-ion batteries (LIBs) have emerged as one of the most promising candidates for green energy solutions [4,5]. However, commercialized graphite anodes used in LIBs are not suitable for electric vehicles (EVs) or portable electronic devices that require high energy density, owing to their low theoretical capacity (372 mAh $g^{-1}$) and poor Li-ion conductivity [6–9]. Recently, numerous studies have been conducted on anode materials that can replace commercial graphite. Metal oxides (e.g., $SnO_2$, $TiO_2$, $Fe_2O_3$, CuO, and $Co_3O_4$) are considered suitable materials because of their high theoretical specific capacities and low operating voltage [10].

Indium(III) oxide ($In_2O_3$) is a promising metal oxide candidate anode material. $In_2O_3$ is an n-type semiconductor that is commonly used in sensors and various electronic devices such as solar cells, flat-panel liquid-crystal displays, and gas detectors. It has relatively higher electric conductivity (1 S $cm^{-1}$) than most other metal oxides (e.g. $SnO_2$, $TiO_2$, $Fe_2O_3$, and $Sb_2O_3$) [11,12]. As an LIB electrode, it has a large theoretical capacity (869 mAh $g^{-1}$, $In_2O_3 + 6Li \rightarrow 2In + 3Li_2O$, $In + 3Li^+ + 3e \rightarrow Li_3In$, corresponding to 9 Li-ions per $In_2O_3$) [13,14]. However, the practical application of $In_2O_3$ in LIB anodes is difficult because of its insufficiently high electrical conductivity (associated with its high band gap (~ 3.5 eV)) and large volume expansion during lithiation, which results in electrode pulverization and cycling performance deterioration. To improve these properties, many researchers have designed nanosized novel structures such as nanosheets [15], nanofibers [16], and nanospheres [17] that can shorten the Li-ion diffusion length and mitigate the volume expansion of the active materials.

The incorporation of various carbonaceous materials into active materials is another efficient strategy for improving the anode performance in batteries. For example, Zhao et al. introduced carbon fibers to $In_2O_3$, which could deliver 435 mAh $g^{-1}$ after 500 cycles at 100 mA $g^{-1}$ [6]. Yang et al. combined graphene and $SnO_2$, thereby achieving good performance with 962 mAh $g^{-1}$ after 50 cycles at 60 mA $g^{-1}$ [18].

* Corresponding authors.
*E-mail addresses:* wonjongjung@gachon.ac.kr (W. Jung), jhhur@gachon.ac.kr (J. Hur).
[1] M. Kim and C. Park made equal contribution.

https://doi.org/10.1016/j.jallcom.2024.174796
Received 17 February 2024; Received in revised form 11 April 2024; Accepted 8 May 2024
Available online 11 May 2024

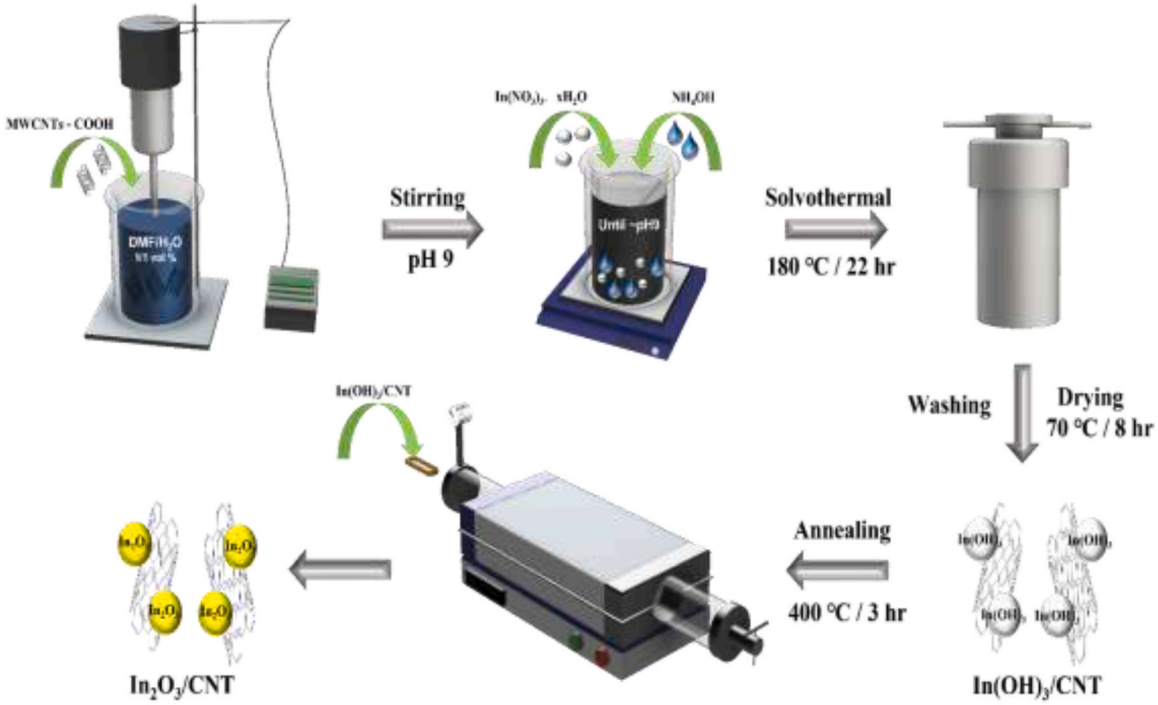


**Fig. 1.** Schematic of $In_2O_3$/CNT synthesis by solvothermal method.

Carbon nanotubes (CNTs) are considered potential carbonaceous materials owing to their exceptional mechanical properties, large surface area, and high electrical conductivity. In particular, a high aspect ratio of 1D CNT easily forms a percolation network structure with a very small loading amount compared to other carbonaceous materials (mostly 0D-based carbon particles), thus achieving a high specific capacity. However, their superiority is often hindered by dispersion difficulties arising from high van der Waals forces, which limit their practical utilization [19].

In this study, we synthesized $In_2O_3$/CNT composites using a facile solvothermal process. The CNTs were homogeneously dispersed by carefully designing the mixing sequence of the precursor materials in a sol-gel process and choosing an appropriate solvent. In addition, the oxygen vacancies in $In_2O_3$ were controlled by the heat-treatment conditions (air vs. Ar environment). A high proportion of oxygen vacancies increases the electrical conductivity of $In_2O_3$ and the number of Li-ion binding sites, thereby enhancing the performance of $In_2O_3$/CNT composite electrodes [20]. As a result, the $In_2O_3$/CNT anode demonstrated good cycling performance (830 mAh $g^{-1}$ after 100 cycles at 200 mA $g^{-1}$) and rate capability (65% retention at 5 A $g^{-1}$ relative to 100 mA $g^{-1}$). In addition, the electrochemical kinetics of the $In_2O_3$-based electrodes were studied to understand the superior electrochemical performance of $In_2O_3$/CNT.

## 2. Experimental

### 2.1. Material synthesis

$In_2O_3$-based composites ($In_2O_3$/CNT) were synthesized via simple solvothermal synthesis followed by heat treatment. Various weights (0.02, 0.083, and 0.174 g) of multi-walled CNTs functionalized by carboxylate groups (CNT-COOH, Cheaptubes Inc., 99%, functional content: ~8.5%; average diameter: 13—18 nm; length: 3—30 μm) were dispersed in 120 ml of co-solvent (N, N-dimethylformamide (DMF):$H_2O$, (1:1, v/v)) using a tip sonicator (Sonics, Vibra-Cell) for 60 min at room temperature. 2 g of $In(NO_3)_3{\cdot}xH_2O$ was added into CNT-dispersed solution and stirred overnight at room temperature. During mixing, a solution pH was adjusted to 9 by slowly dropping $NH_4OH$ (Alfa Aesar, 25%) into the above solution. The resulting solution was transferred into a 200 ml Teflon-lined stainless-steel autoclave and temperature was maintained at 180 °C for 22 h for the following sol-gel reaction.

$$In(NO_3)_3 \bullet xH_2O + 3NH_4OH \xrightarrow[H_2O]{}{}_{/DMF} In(OH)_3\downarrow + 3NH_4NO_3 \quad (1)$$

$$2In(OH)_3 \xrightarrow{\Delta} In_2O_3 + 3H_2O \quad (2)$$

Subsequently, the as-synthesized sample was naturally cooled to room temperature, collected by centrifugation (8000 rpm for 5 min), and thoroughly washed five times with deionized water and ethanol. The precipitates were dried at 80 °C in the vacuum oven for 12 h and then annealed at 400 °C for 3 h (ramping rate: 10 °C/min) in air or Ar atmosphere. These were denoted as $In_2O_3$/CNT_Air and $In_2O_3$/CNT_Ar, respectively. Separately, pure $In_2O_3$ was prepared using the same procedure (annealed under air) but without CNT addition (denoted as $In_2O_3$). The above procedure is illustrated in Fig. 1.

### 2.2. Characterization

The crystal structure of as-prepared products was characterized using X-ray diffraction (XRD, Rigaku D/max 2200 PC V diffractometer) operating with Cu Kα radiation ($\lambda = 1.5406$ Å) at a scan rate of 2° $min^{-1}$, with 2θ scan range of 20°−80°. The chemical bonding states were analyzed using X-ray photoelectron spectroscopy (XPS, Theta Probe Instrument (Thermo Fisher Scientific, UK)). The powder morphology was observed by field-emission scanning electron microscopy (SEM, Hitachi S4700 at the Smart Materials Research Center for IoT at Gachon University for its instrumental support) and transmission electron microscopy (TEM, JEOL JEM-2100 F) with EDX mapping. The $N_2$ adsorption and desorption isotherms of the samples were obtained using a micrometric instrument (ASAP 2020). The surface areas of the fabricated samples were analyzed using the Brunauer-Emmett-Teller (BET) method. Raman spectral analysis was performed to obtain chemical and structural information (Olympus BX51). Thermogravimetric analysis (TGA, Perkin Elmer TGA 4000) was used to determine the weight content of CNT and $In_2O_3$ in the $In_2O_3$/CNT composite. UV–visible (UV-Vis)

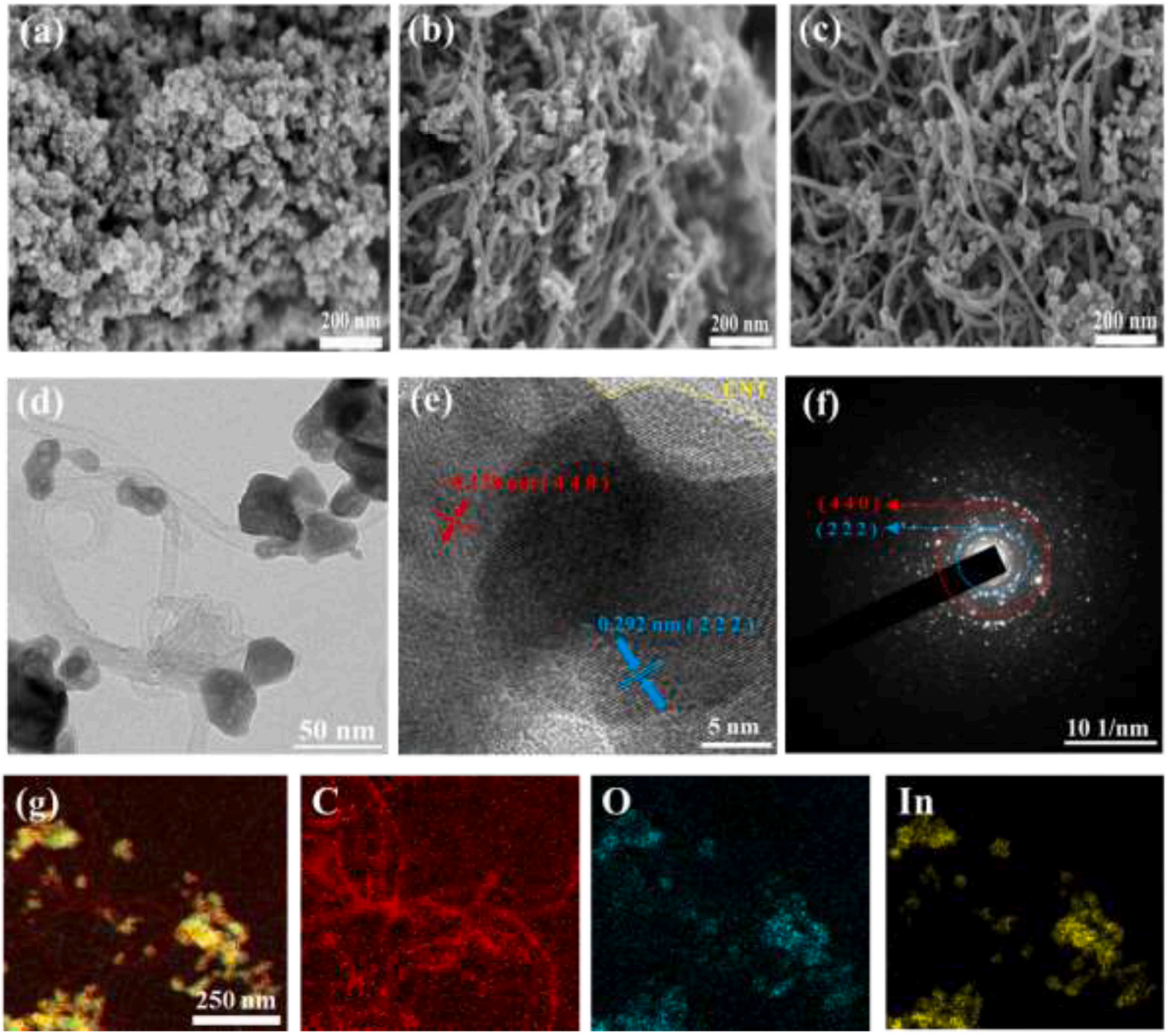


**Fig. 2.** SEM images of (a) $In_2O_3$, (b) $In_2O_3$/CNT_Air, (c) $In_2O_3$/CNT_Ar, (d) TEM, (e) HRTEM, (f) SAED pattern images, and (g) EDX mapping of $In_2O_3$/CNT_Ar.

spectrometry (LAMDA750, Perkin Elmer, Waltham, USA) was used to compare the CNT dispersions in different solvents.

### 2.3. Electrode fabrication

The slurry was prepared by mixing the as-synthesized active material, binder (polyacrylic acid, average Mv ~450,000, Sigma-Aldrich), and conductive material (Super P, 99+%, metal basis, Alfa Aesar) in absolute ethanol (99.9%, Daejung) at a ratio of 70:15:15 (w/w/w) for 24 h with stirring. The slurry was cast on a Cu foil using doctor blade with a mass loading of 1−2 mg and then dried in vacuum oven at 70 °C overnight. A coin-type cell (CR 2032) was used for electrochemical measurements. The fabricated electrode was punched into a circular shape (diameter of 12 mm) and used as the working electrode. Li foil (99.9%, metal basis, thickness = 0.75 mm, diameter = 12.5 mm, Alfa Aesar) was used as the counter electrode. A 1 M $LiPF_6$ solution (dissolved in ethylene carbonate (EC)/ dimethyl carbonate ((DEC), 1:1 v/v) and polyethylene membrane were used as the electrolyte and separator, respectively. All the coin cells were assembled in an Ar-filled glove box.

### 2.4. Electrochemical measurements

Galvanostatic charge/discharge (GCD) tests were carried out in the voltage range of 0.01−3.0 V (vs. $Li/Li^+$) using a battery cycler (WBCS3000, Won-A-Tech, South Korea) at various current densities. Cyclic voltammetry (CV) was performed in the voltage range of 0.01−3.0 V (vs. $Li/Li^+$) at different voltage scan rates with a ZIVE MP1 workstation. The electrochemical impedance spectroscopy (EIS) was performed in the frequency range 100 kHz to 0.1 Hz at an alternative current amplitude of 5 mV with a ZIVE MP1 workstation. All measurements were conducted on half-cell configurations at room temperature.

## 3. Results and discussion

### 3.1. Characterization of $In_2O_3$, $In_2O_3$/CNT_Air, and $In_2O_3$/CNT_Ar powder

The $In_2O_3$/CNT composite was prepared using a solvothermal process and heat treatment (Fig. 1). Fig. 2**a**−**c** show the morphologies of the

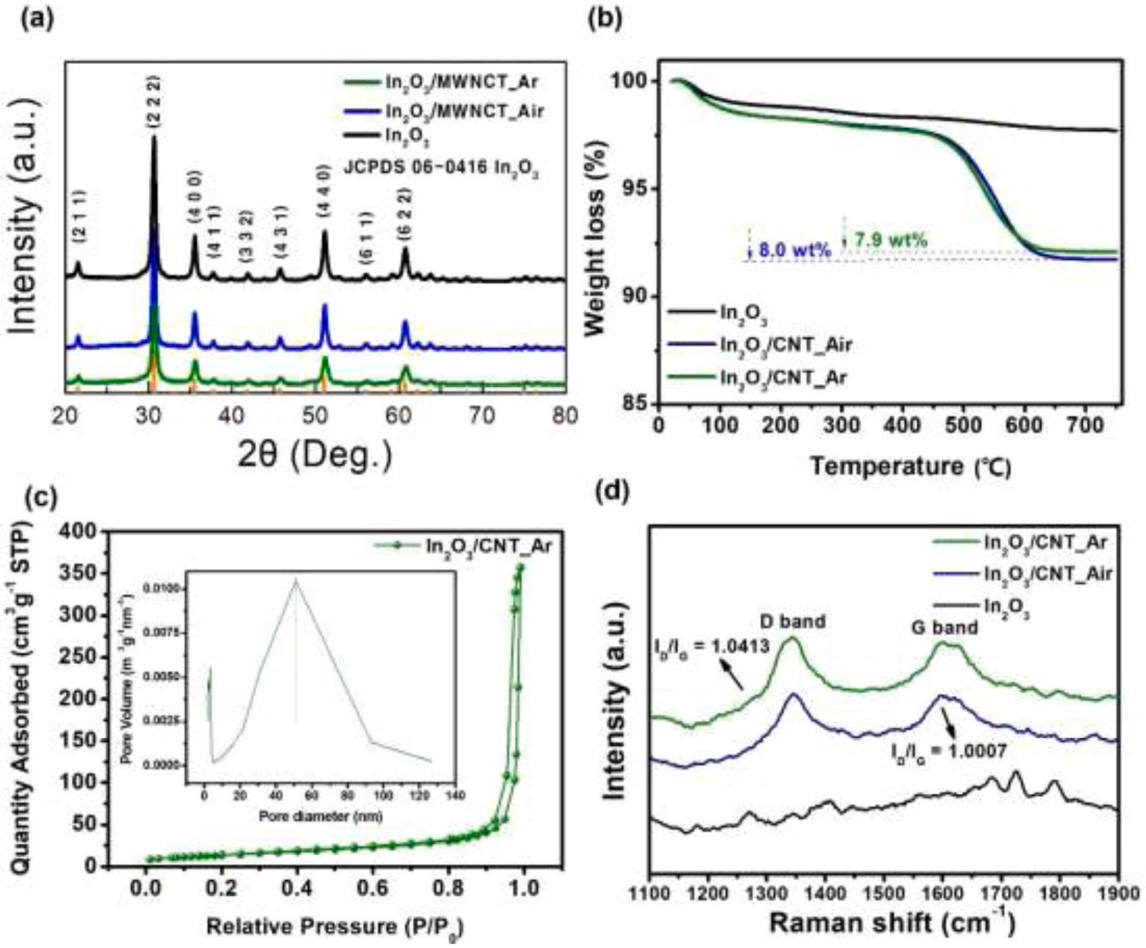


**Fig. 3.** (a) XRD analysis, (b) TGA curves in air environment, (c) Nitrogen adsorption-desorption isotherms and the corresponding pore-size distribution curves (inset) for the $In_2O_3$/CNT_Ar, and (d) Raman spectra of the samples.

as-synthesized $In_2O_3$, $In_2O_3$/CNT_Air, and $In_2O_3$/CNT_Ar. According to the particle size distribution analysis (Fig. S1), the diameter of the $In_2O_3$ nanoparticles (NPs) was in the range of 5–55 nm. Notably, the particle size of $In_2O_3$/CNT_Ar is slightly greater than that of $In_2O_3$/CNT_Air. This seems to be associated with different CNT defect density. Because $In_2O_3$ nanoparticles are grown on the CNT surface during sol-gel process, the nucleation and growth of $In_2O_3$ can be influenced by the CNT defect density. It is speculated that the defects on CNT facilitate more effective bonding between $In_2O_3$ and CNT and promote $In_2O_3$ nucleation and growth. Due to higher CNT defect density of $In_2O_3$/CNT_Ar than that of $In_2O_3$/CNT_Air (which will be discussed later), the $In_2O_3$ particle size of $In_2O_3$/CNT_Ar is greater than that of $In_2O_3$/CNT_Air. From the results in Fig. 3**d** (Raman spectra), the CNT defect density in $In_2O_3$/CNT_Ar is higher than that of $In_2O_3$/CNT_Air. CNTs were introduced into $In_2O_3$ because of their (i) high aspect ratio that shortens the Li-ion diffusion pathways, ii) high electronic conductivity (49.5 S $cm^{-1}$) [21], and iii) good mechanical properties (Young's modulus: 10 GPa) [22]. However, homogeneously dispersing CNTs and preventing their aggregation is challenging due to their high van der Waals forces. To resolve this issue, we used CNT-COOH, in which the carboxylate functional groups render electrostatic repulsion and reduce CNT aggregation. The selection of an appropriate solvent (DMF/$H_2O$ co-solvent) is another important factor in CNT dispersion. Indeed, we confirmed superior CNT dispersion with the DMF/$H_2O$ co-solvent compared with pure ethanol (Fig. S2). At the same concentration, CNTs dispersed in the DMF/$H_2O$ co-solvent showed higher absorbance in the measured wavelength range (300—1100 nm) than those dispersed in pure ethanol (Fig. S2a). Additionally, photographs of the dispersed CNTs after 3 days of incubation indicate more homogeneous CNT dispersion in the co-solvent (Fig. S2b-S2c). This enhanced dispersion was attributed to the high polarity of DMF, which induces polar interactions with the carboxyl groups (–COOH) of the CNT [23,24]. In addition, $In_2O_3$ NPs and CNT were mixed by dissolving $In_2O_3$ precursor ($In(NO_3)_3{\cdot}xH_2O$) rather than directly dispersing $In_2O_3$ NPs in CNT-dispersed solution for the uniform mixture of two components. The use of CNT-COOH, a co-solvent, and dissolution of the $In_2O_3$ precursor in the CNT-dispersed solution ensured good CNT dispersion and uniformly distributed $In_2O_3$ NPs and CNTs. Fig. 2**b**—**2c** confirm the homogeneous dispersion of $In_2O_3$ and CNT in $In_2O_3$/CNT without significant aggregation. From this morphology, it is expected that individual active $In_2O_3$ NPs can participate equally in electrochemical reactions, and Li-ions can easily diffuse into the $In_2O_3$ NPs. Fig. 2**d**—**2 g** show the TEM, high-resolution TEM (HRTEM), selected area electron diffraction (SAED), and EDX mapping of $In_2O_3$/CNT_Ar. The $In_2O_3$ NPs adhered strongly to the CNT via their functional moieties (Fig. 2**d**). The HRTEM image shows interplanar distances of ~0.178 and 0.292 nm, corresponding to the (440) and (222) planes of the $In_2O_3$ lattice, respectively (Fig. 2**e**). These planes were also confirmed in the SAED pattern (Fig. 2**f**). The EDX mapping images show a uniform distribution of the elements (In, O, and C) in $In_2O_3$/CNT (Fig. 2**g**).

Fig. 3**a** shows the XRD patterns of the as-prepared $In_2O_3$, $In_2O_3$/CNT_Air, and $In_2O_3$/CNT_Ar powders. The peaks observed at 21.5°, 30.6°, 35.5°, 37.7°, 41.2°, 45.7°, 51°, 56°, and 60.7° correspond to the (2 1 1), (2 2 2), (4 0 0), (4 1 1), (3 3 2), (4 3 1), (4 4 0), (6 1 1), and (6 2 2) lattice planes of $In_2O_3$, respectively. Comparing this result with the XRD

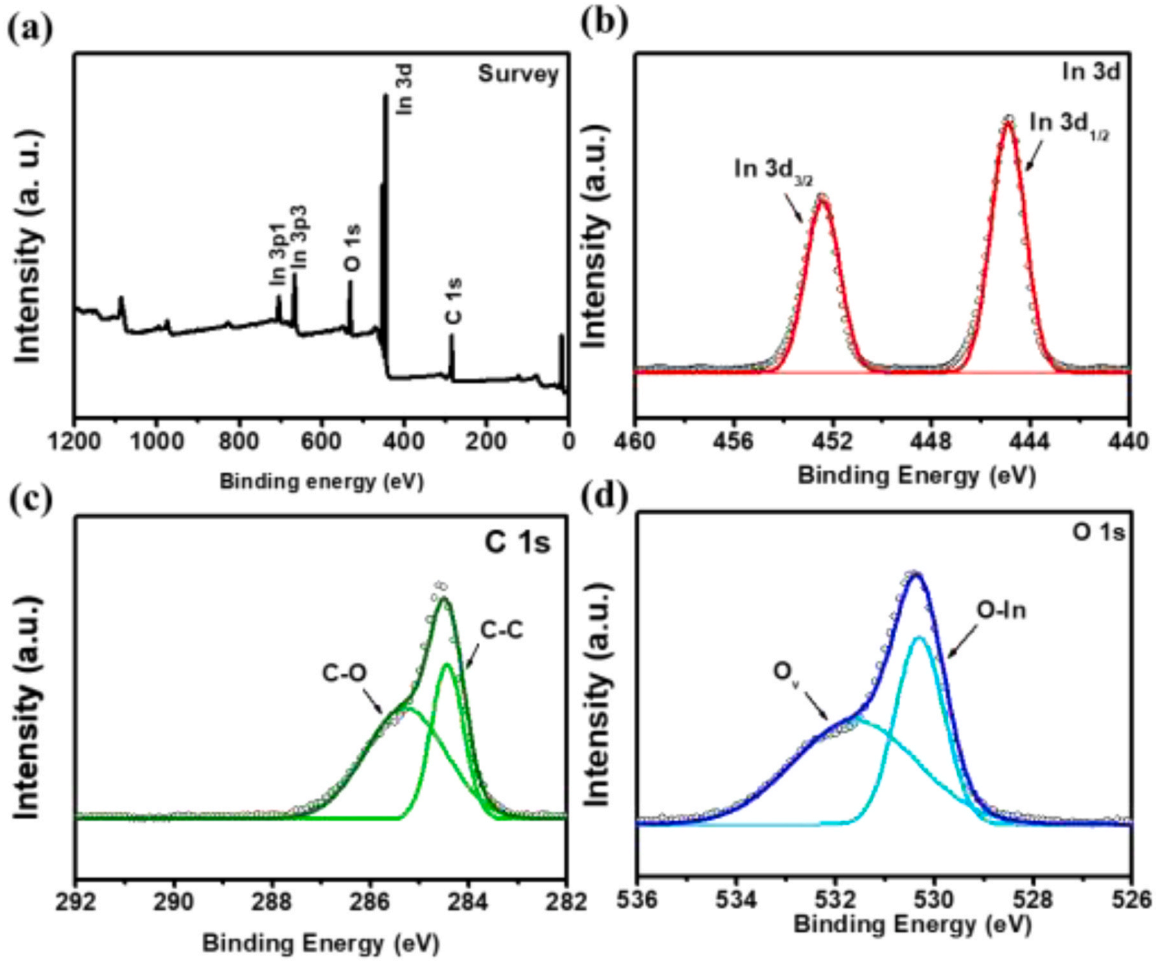


**Fig. 4.** (a) XPS survey and (b) In 3d, (c) C 1 s, and (d) O 1 s spectra of $In_2O_3$ /CNT_Ar.

pattern of $In(OH)_3$/CNT (before thermal annealing, Fig. S3) confirmed the complete and successful conversion of $In(OH)_3$ to $In_2O_3$ through thermal annealing without any residue. Notably, CNT peaks were not observed because of the much higher $In_2O_3$ content (92 wt%) compared to the CNT (8 wt%) (the exact CNT content is discussed later in the TGA analysis in Fig. 3**b**). In addition, as the number of oxygen vacancies increased, the crystal lattice of $In_2O_3$ became more disordered, and structural rearrangement occurred. This can be confirmed from the slight left shift of the (222) peak of $In_2O_3$/CNT_Ar compared to that of $In_2O_3$/CNT_Air (Fig. S4), suggesting that the lattice interplanar spacing expanded owing to oxygen vacancies, according to *Bragg's law* [25,26]. Fig. 3**b** displays TGA analysis of the $In_2O_3$, $In_2O_3$/CNT_Air, and $In_2O_3$/CNT_Ar from 25 °C to 750 °C in air atmosphere. All of the samples showed a gradual weight decrease until ~400 ℃ which is associated with the decomposition of residual water and adsorbed organic molecules. After ~400 ℃, the weight of both the $In_2O_3$/CNT_Air and $In_2O_3$/CNT_Ar were rapidly decreased owing to the CNT combustion ($C + O_2 \rightarrow CO_2$) [27]. The weight loss for both the $In_2O_3$/CNT_Air and $In_2O_3$/CNT_Ar were similar (~8%) because of the same amount of CNT added during the solvothermal synthesis. This can rule out the effect of the CNT quantity, which can cause differences in the electrochemical performance between $In_2O_3$/CNT_Air and $In_2O_3$/CNT_Ar. Based on these results, the theoretical capacity of the $In_2O_3$/CNT composite was calculated to be 829.24 mAh $g^{-1}$ (869 mAh $g^{-1}$ × 0.92 + 372 mAh $g^{-1}$ × 0.08 = 829.24 mAh $g^{-1}$, theoretical capacity: $In_2O_3$ (869 mAh $g^{-1}$) [13, [28]and CNT (372 mAh $g^{-1}$). The pore size distribution obtained by the BET analysis (Fig. 3**c**) revealed that $In_2O_3$/CNT_Ar exhibited slightly larger pores (30–40 nm) than $In_2O_3$/CNT_Air (20–30 nm) (Fig. S5). The mesoporous structures of $In_2O_3$/CNT_Ar and $In_2O_3$/CNT_Air provided a large surface area and shortened the Li-ion pathways, enabling high capacity and rapid Li-ion diffusion.

Raman spectral analysis was conducted to further understand the structural characteristics, as shown in Fig. 3**d**. The D and G bands reflect defects and vibrations in $sp^2$-bonded carbon of carbon-based materials. $In_2O_3$/CNT_Ar exhibited a higher $I_D/I_G$ value (~1.04) than $In_2O_3$/CNT_Air (~1.00). Defects generally occur during the transition from planar $sp^2$ to $sp^3$ bonding, which may facilitate the formation of favorable binding sites for $In_2O_3$ NPs in the sol-gel process [29,30]. During the nucleation and growth of $In_2O_3$ particles during sol-gel process, $In_2O_3$ particles tend to be more strongly bound on the defect sites of the CNTs. This is because of the reduced activation energy when introducing new functional groups or foreign species on CNT defect sites [30–32]. Therefore, it can be thought that overall binding stability of $In_2O_3$ particles on the $In_2O_3$/CNT_Air (with more CNT defects) is higher than that on the $In_2O_3$/CNT_Ar (with less CNT defects). The strong binding between the $In_2O_3$ NPs and CNT in $In_2O_3$/CNT_Ar is expected to enhance the mechanical stability of the composite [33].

X-ray photoelectron spectroscopy (XPS) was used to investigate the chemical bonding states of $In_2O_3$/CNT_Ar (Fig. 4). The XPS survey spectra (Fig. 4**a**) indicated the presence of In, O, and C, which is consistent with the EDX mapping results (Fig. 2**g**). In In 3d orbital level, peaks at 452.4 and 444.9 eV were assigned to In $3d_{5/2}$ and In $3d_{3/2}$ for $In_2O_3$, respectively (Fig. 4**b**) [34]. The peaks at 285.27 and 284.44 eV in C 1 s spectra corresponded to $sp^3$ bonding of C-C and $sp^2$ bonding of C═C, respectively (Fig. 4**c**) [35]. In Fig. 4**d**, the peaks observed at 530.3 and 531.6 eV in the O 1 s level spectrum represent the chemical bonding

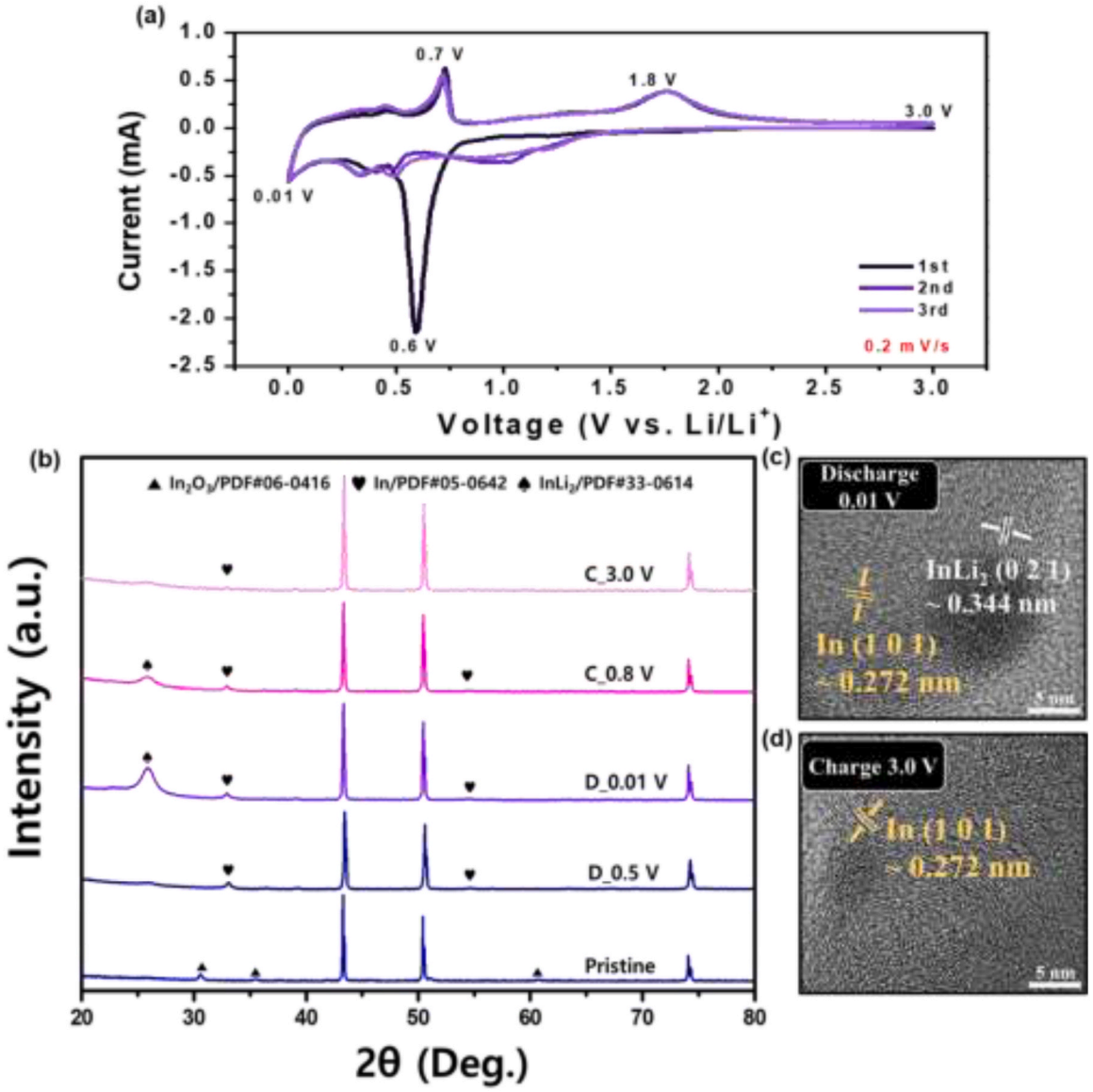


**Fig. 5.** (a) Cyclic voltammogram of $In_2O_3$/CNT_Ar at a scan rate of 0.2 mV $s^{-1}$ (b) ex-situ XRD analysis of $In_2O_3$/CNT_Ar during 1st charge/discharge, ex-situ HRTEM of $In_2O_3$/CNT_Ar at fully (c) discharged and (d) charged state.

states of In-O-In and oxygen vacancies, respectively [17]. From the deconvolution of the O 1 s spectra (Fig. S6), the oxygen vacancy of $In_2O_3$/CNT_Ar (58.57%) was higher than that of $In_2O_3$/CNT_Air (48.15%). This is due to the different thermal annealing conditions; the number of oxygen vacancies decreased for $In_2O_3$/CNT_Air because of the relatively oxygen-rich environment in the air atmosphere. In contrast, more oxygen defects were formed in $In_2O_3$/CNT_Ar in the absence of an oxygen atmosphere. More oxygen defects in $In_2O_3$/CNT_Ar are expected to increase the number of reaction sites in active $In_2O_3$, resulting in a higher capacity. The presence of oxygen vacancy in $In_2O_3$ NPs was further confirmed by the photoluminescence measurement. As shown in Fig. S7, two different PL regions are generally observed in metal oxides, so-called near band emission (NBE) and deep level emission (DLE).[36, 37] NBE represents the radiative recombination based on electron transition associated with energy bandgap. DLE originates from the subgap energy levels of various defect sites including oxygen vacancy ($V_O$). [38] As reported in previous literatures, in the case of $In_2O_3$, the PL emission spectra range from 400 to 500 nm result from the existence of singly ionized $V_O$ species, [39,40] and the PL signal from 500 to 650 nm wavelengths is due to the deep $V_O$ levels of $In_2O_3$. [41,42] As displayed in our PL results (Fig. S7), our $In_2O_3$ NPs exhibited broad range of DLE PLs indicating subgap energy transitions originating from $V_O$, which clearly demonstrates the presence of $V_O$ defects in the $In_2O_3$ NPs.

### 3.2. Electrochemical performance

To study the electrochemical reaction behavior of $In_2O_3$/CNT during charge/discharge, the cyclic voltammetry (CV) was conducted at a scan rate of 0.2 mV $s^{-1}$ in the voltage range from 0.01 to 3.0 V (vs. $Li/Li^+$) (Fig. 5**a**). In the first cycle, a strong cathodic peak at 0.6 V showed the conversion reaction of $In_2O_3$ to metallic In and the formation of SEI film ($In_2O_3 + 6Li \rightarrow 2In + 3Li_2O$). This electrochemical reaction is believed to be irreversible; thus, this peak did not appear in subsequent cycles. This electrochemical reaction was confirmed by the XRD peaks at 33° and 55° (corresponding to In) in the D-0.5 V in Fig. 5**b**. In the subsequent cycles, this cathodic peak shifted and splitted into 0.35 and 0.48 V. These peaks indicate the formation of Li-In alloys [10]. At the fully discharged state (D-0.01 V in Fig. 5**b**), XRD results suggest the formation of a Li-In alloy ($In + xLi^+ + xe \rightarrow Li_xIn$). Correspondingly, the XRD patterns in the fully discharged state (0.01 V) exhibited the characteristic peaks of the $Li_xIn$

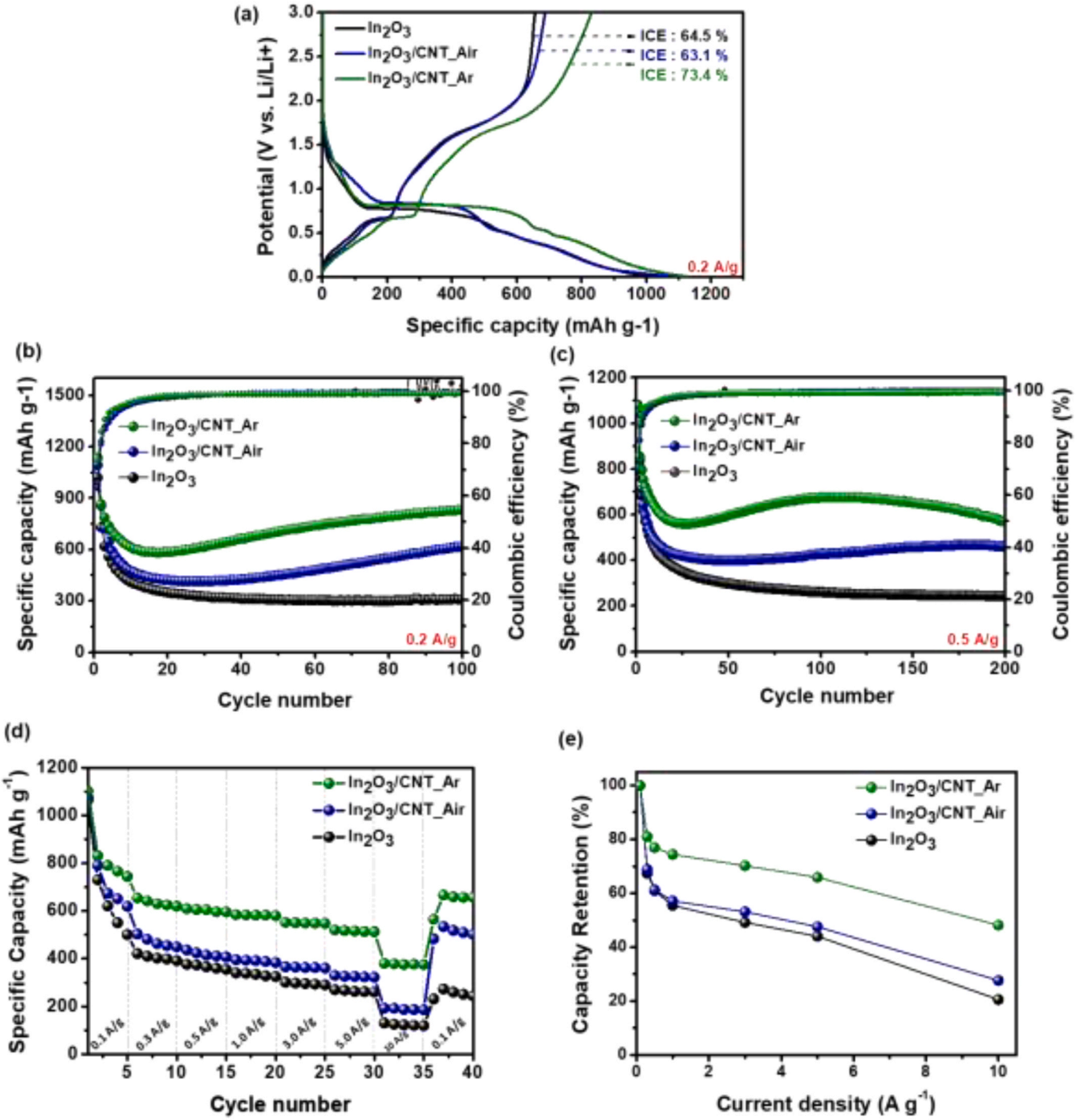


**Fig. 6.** Electrochemical performance: (a) Voltage profiles (0.2 A $g^{-1}$ with 0.01–3.00 V (*vs.* Li/Li+), long-term cycling performance at current densities of (b) 0.2 A $g^{-1}$ (c) 0.5 A $g^{-1}$. (d) Rate capability and (e) normalized capacity retention from rate capability.

alloy. Additionally, ex situ high-resolution transmission electron microscopy (HRTEM) confirmed the presence of the $Li_xIn$ alloy along with residual In phases (Fig. 5**c**). During the charging process in the first cycle, two anodic peaks appeared at 0.72, and 1.76 V (Fig. 5**a**). These peaks indicate partial Li dealloying reaction ($Li_xIn \rightarrow In + xLi^+ + xe$). In the fully charged state (3.0 V), the previously observed diffraction peaks of $Li_xIn$ completely disappeared and In peak still remained in the XRD patterns, indicating a further de-alloying reaction ($Li_xIn \rightarrow In + xLi^+ + xe$). HRTEM analysis (Fig. 5**d**) further confirmed the remaining In phases, with the overall electrochemical reactions summarized in (3)–(5) [43,44]. After first cycle, active In undergoes reversible electrochemical reactions as follows:

First discharge process:

$$In_2O_3 + 6Li^+ \rightarrow 2In + 3Li_2O \text{ at } 0.6 \text{ V (vs. } Li/Li^+) \quad (3)$$

$$In + xLi^+ + xe \rightarrow Li_xIn \text{ at } 0.01 \text{ V (vs. } Li/Li^+) \quad (4)$$

First charge process:

$$Li_xIn \rightarrow In + xLi^+ + xe \text{ at } 0.7 \text{ and } 1.8 \text{ V (vs. } Li/Li^+) \quad (5)$$

After second discharge process:

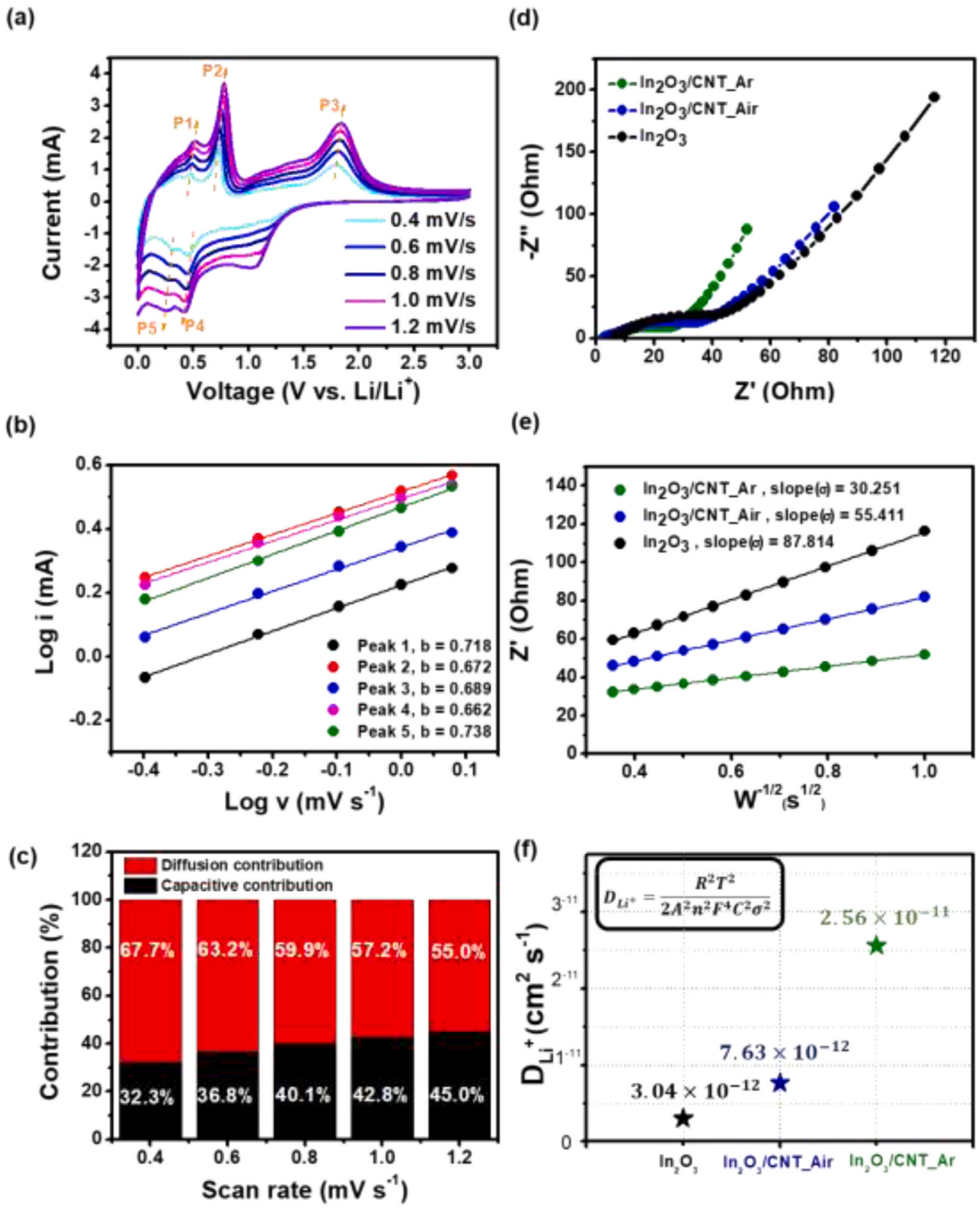


**Fig. 7.** (a) Cyclic voltammetry at various scan rates, (b) linear fitting of *log v vs. log i* to calculate the *b* value, and (c) contribution ratio between capacitive and diffusion-controlled behavior at various scan rates for the $In_2O_3$/CNT_Ar. (d) Nyquist plots, (e) linear fitting of $\omega^{-0.5}$ versus *Z'* plot based on EIS measurement for Warburg factor estimation, and (f) Li-ion diffusion coefficient.

$$In + xLi^+ + xe \rightarrow Li_xIn \quad (6)$$

After second charge process:

$$Li_xIn \rightarrow In + xLi^+ \quad (7)$$

Fig. 6**a** shows voltage profiles of all electrodes ($In_2O_3$, $In_2O_3$/CNT_Air, and $In_2O_3$/CNT_Ar) in the first cycle at a current density of 0.2 A $g^{-1}$ over the voltage range from 0.01 to 3.0 V (vs. $Li/Li^+$). The initial discharge/charge capacities of the $In_2O_3$, $In_2O_3$/CNT_Air, and $In_2O_3$/CNT_Ar were 1016.77/656.07 mAh $g^{-1}$, 1092.26/687.63 mAh $g^{-1}$, and 1131.19/830.29 mAh $g^{-1}$, corresponding to the initial coulombic efficiencies (ICE) of 64.5%, 63.0% and 73.4% for $In_2O_3$, $In_2O_3$/CNT_Air, and $In_2O_3$/CNT_Ar, respectively. The low ICEs of the electrodes are attributed to the formation of a solid electrolyte interface (SEI) film on the electrode surface. Nevertheless, the $In_2O_3$/CNT_Ar electrode exhibited the highest ICE (73.4%) compared to other electrodes (64.5 and 63%). When comparing the CEs for up to 10 cycles, $In_2O_3$/CNT_Ar showed consistently higher CEs than the other electrodes, demonstrating superior reversibility (Table S1). The long-term cycling performance of $In_2O_3$-based electrodes was tested from GCD measurement in the voltage range from 0.01 to 3.0 V (vs. $Li/Li^+$) with a half-cell

configuration (Fig. 6**b**−**6c**). The specific discharge capacities of $In_2O_3$, $In_2O_3$/CNT_Air, and $In_2O_3$/CNT_Ar were 306, 617, and 830 mAh $g^{-1}$ after 100 cycles at a current density of 0.2 A $g^{-1}$ and 243, 458, and 570 mAh $g^{-1}$ after 200 cycles at a current density of 0.5 A $g^{-1}$, respectively. $In_2O_3$/CNT_Ar showed the highest specific capacity of all the $In_2O_3$-based electrodes. The good electrochemical performance of $In_2O_3$/CNT_Ar is associated with the following synergetic attributes: (i) $In_2O_3$ NPs provide high surface area and shorter Li-ion diffusion path (ii) Well-distributed CNTs prevent $In_2O_3$ NPs aggregation and mitigate the volume change during charge/discharge [45] (iii) Appropriate oxygen vacancies promote ionic conductivity through elevated Li-ion diffusion coefficient, which serves as a significant contributing factor to higher specific capacity [46] iv) A large number of pores in $In_2O_3$/CNT_Ar alleviates the structural stress during charge/discharge [47]. During the initial cycles, specific capacities gradually decreased due to SEI formation and the unstable buffering role of CNTs. In contrast, after approximately 20 cycles, the specific capacities of the $In_2O_3$/CNT composites ($In_2O_3$/CNT_Air and $In_2O_3$/CNT_Ar) gradually increased. This tendency was more pronounced for the $In_2O_3$/Ar in both current densities (200 and 500 mA $g^{-1}$ in Figs. 6**b** and 6**c**). This phenomenon often occurs in metal oxide anodes and is associated with additional pseudo-capacitor formation due to electrolyte decomposition, which acts as additional Li-ion storage (so-called electrode activation) [48]. In the case of $In_2O_3$/CNT_Ar, the higher oxygen vacancy defects function as redox reaction sites, thereby enhancing the electrode activation more effectively [49]. Additionally, an appropriate concentration of oxygen vacancies provides high conductivity, resulting in high reversible capacity and Li-ion mobility. Therefore, the $In_2O_3$/CNT_Ar sample did not exhibit visible fine cracks and maintained a relatively smooth surface compared with the other samples (Fig. S8). Another reason for the gradual increase in capacity is the highly porous nature of the $In_2O_3$/CNT electrodes. As confirmed by BET analysis, the specific surface area (SSA) of the $In_2O_3$, $In_2O_3$/CNT_Air, and $In_2O_3$/CNT_Ar were 22.97, 44.98, and 72.88 $m^2$ $g^{-1}$, respectively. The higher SSA of $In_2O_3$/CNT_Air and $In_2O_3$/CNT_Ar than that of $In_2O_3$ is attributed to the presence of porous CNT with high surface area. The higher SSA of $In_2O_3$/CNT_Ar than that of $In_2O_3$/CNT_Air can be associated with more CNT defects in $In_2O_3$/CNT_Ar as confirmed from Raman spectroscopy measurements (Fig. 3**d**). The highest SSA of $In_2O_3$/CNT_Ar can increase accessible active sites for Li-ions, resulting in the increased capacity. Figs. 6**d** and 6**e** show the rate capability and normalized capacity retention of $In_2O_3$-based electrodes at current densities of 0.1−5 A $g^{-1}$. Consistent with the cycling performance, $In_2O_3$/CNT_Ar exhibited higher capacities than the other electrodes at all current densities (Fig. 6**d**). The average specific capacities of $In_2O_3$/CNT_Ar electrode were 791, 630, 594, 575, 546, and 517 mAh $g^{-1}$ at current densities of 0.1, 0.3, 0.5, 1.0, 3.0, and 5.0 A $g^{-1}$, corresponding to the capacity retentions of 100%, 80%, 75%, 73%, 69%, and 65%, respectively (Fig. 6**e**). When returning to the low current density of 0.1 A $g^{-1}$, the recovered capacity was 83%, indicating highly reversible properties even after undergoing harsh current density conditions. The good performance of $In_2O_3$/CNT_Ar was attributed to its micro and macroscopic structural features, excellent charge transfer kinetics, and high electrical conductivity. Additionally, a high concentration of oxygen vacancies provided free charges and improved the electronic conductivity, thus enhancing the rate capability of $In_2O_3$/CNT_Ar. Furthermore, to determine the optimum ratio of $In_2O_3$ to CNT in $In_2O_3$/CNT_Ar, the cycling performances of $In_2O_3$/CNT_Ar at various ratios were measured. On the basis of precursor ratio ($In(NO_3)_3{\cdot}xH_2O$: CNT), the $In_2O_3$/CNT_Ar containing 4 wt% CNT ($In(NO_3)_3{\cdot}xH_2O$: CNT = 96:4 (w:w)) showed the best performance (Fig. S9), which corresponds to 8 wt% CNT in the final composite ($In_2O_3$:CNT = 92:8 (w:w)), as estimated by TGA (Fig. 3**b**).

To investigate the electrochemical kinetics $In_2O_3$/CNT_Ar, CV analysis was conducted at various scan rates (0.4, 0.6, 0.8, 1.0, and 1.2 mV $s^{-1}$) in the range of 0.01−3.00 V (Fig. 7**a**). As the scan rate increased, the peak current also increased. The current dependence of the scan rate is expressed by the following electrochemical formula [50]

$$i = av^b \tag{8}$$

$$\log i = b\log v + \log a \tag{9}$$

where $i$ is the current, $v$ is the scan rate, and $a$ and $b$ are parameters associated with this equation. Specifically, $b$ values of 0.5 and 1 correspond to diffusion (battery, sharp peak shape) and surface-controlled (capacitor, rectangular shape) reactions, respectively. The b values of the five peaks in Fig. 7**a** obtained from the linear fitting of the log v vs. log i plot were 0.718, 0.672, 0.689, 0.662, and 0.738 (Fig. 7**b**), indicating contributions from both diffusion-controlled and pseudo-capacitive behavior. Their quantitative contributions can be obtained using Dunn's method as follows [1]

$$i = k_1 v + k_2 v^{1/2} \tag{10}$$

$$iv^{-1/2} = k_1 v^{1/2} + k_2 \tag{11}$$

where $k_1$ and $k_2$ are parameters associated with the diffusion-controlled and pseudo-capacitive reactions, respectively. These contributions can be quantified from the linear fitting of $iv^{-1/2}$ vs. $v^{1/2}$ graph in Fig. S10. As shown in Fig. 7**c**, the contribution of the pseudo-capacitance increased with an increase in the scan rate. The same analysis was applied to the control samples ($In_2O_3$ and $In_2O_3$/CNT_Air). As shown in Fig. S11, the contribution of the pseudo-capacitance exhibited an increasing trend with increasing scan rate to all samples. Among them, $In_2O_3$/CNT_Ar demonstrated the highest current values with various scan rates, indicating superior electrochemical kinetics.

To gain further insight into the electrochemical kinetics, EIS analysis was performed on $In_2O$, $In_2O_3$/CNT_Air, and $In_2O_3$/CNT_Ar. As shown in Fig. 7**d** and Fig. S12-S13, the Nyquist plots and EIS circuits of all the samples were acquired before cycling and upon reaching a fully charged state (3.0 V) after 30 cycles, where $R_b$ is the intrinsic resistance derived from the internal bulk materials inside the cell, $R_{SEI}$ is the resistance value attributed to the SEI layer, CPE is utilized as a constant phase element to complement a non-ideal capacitor, $R_{ct}$ is the charge transfer resistance related to the electrochemical kinetics, and W is the Warburg impedance appearing in the low-frequency region behind the semicircle, which is associated with Li-ion diffusion [51]. As summarized in Table S2, the $R_{ct}$ values of $In_2O_3$, $In_2O_3$/CNT_Air, and $In_2O_3$/CNT_Ar were 89.2, 57.7, 36.1 Ω before cycling and 71.2 Ω, 48.9 Ω, and 34.7 Ω after 30 cycles, respectively, further demonstrating that $In_2O_3$/CNT_Ar has the lowest $R_{ct}$ value. The Li-ion diffusion coefficient was obtained using the following equation [52]

$$Z_{real} = R_s + R_{ct} + \sigma\omega^{-0.5} \tag{12}$$

$$D_{Li^+} = \frac{R^2T^2}{2A^2n^4F^4C^2\sigma^2} \tag{13}$$

where R, T, A, n, F, C, and σ correspond to gas constant, absolute temperature, the number of Li-ions involved in the electrochemical reaction, the Faraday constant, concentration of lithium ions in the electrolyte, and the parameter associated with Warburg impedance, respectively. First, σ value (slope) was obtained through linear fitting with $w^{-1/2}$ vs. $Z_{real}$ (Fig. 7**e**), then $D_{Li+}$ was determined with known parameters and obtained σ for all the samples (Fig. 7**f**). The $D_{Li+}$ of $In_2O_3$, $In_2O_3$/CNT_Air, and $In_2O_3$/CNT_Ar were $3.04 \times 10^{-12}$, $7.63 \times 10^{-12}$, and $2.56 \times 10^{-11}$ $cm^2/s$, respectively, indicating that the diffusion coefficient of $In_2O_3$/CNT composites was at least eight times greater than that of pure $In_2O_3$. This phenomenon can be explained by the porous structure and presence of CNT along with the nanosized active $In_2O_3$ particles, which significantly shorten the Li-ion pathways and construct an efficient percolation network. The enhanced Li-ion transport efficiency was further confirmed by the galvanostatic intermittent titration technique

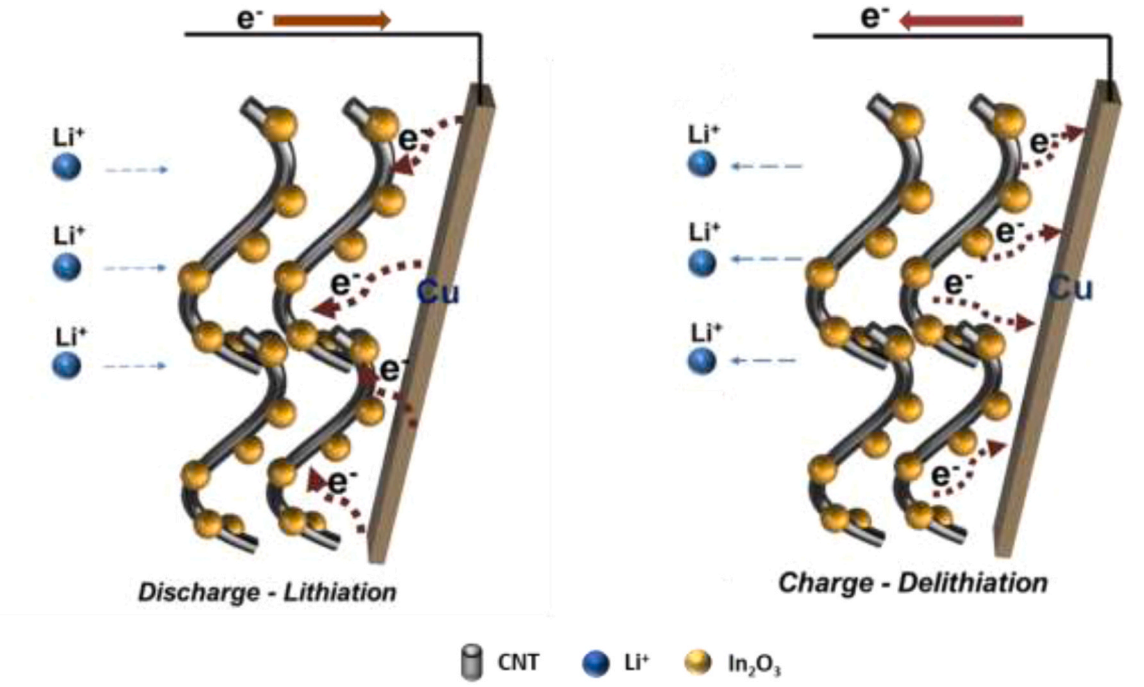


**Fig. 8.** Schematic of electrochemical reaction of $In_2O_3$/CNT_Ar electrode in half cell.

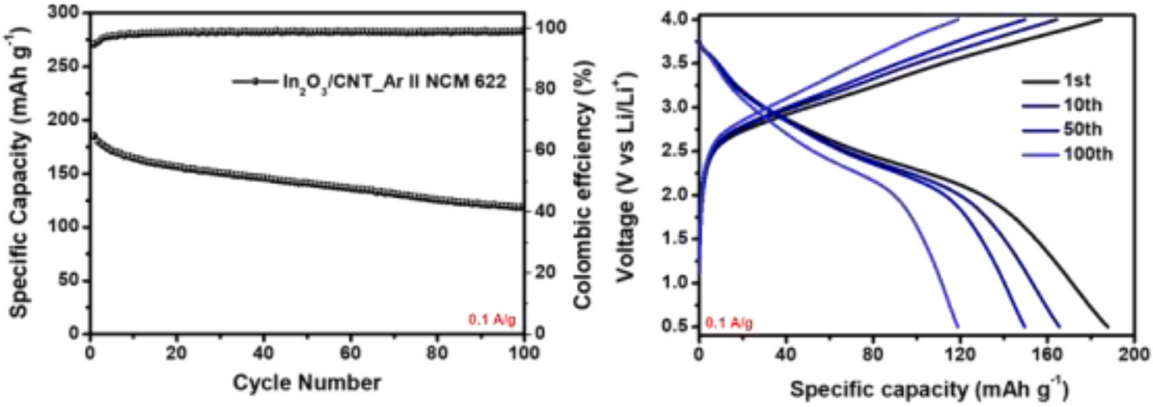


**Fig. 9.** (a) Cycling performance, (b) voltage profile of the $In_2O_3$/CNT_Ar||NCM622 full battery.

(GITT) [53,54]. Fig. S14a shows voltage-time curves for three different electrodes. Lithium ion diffusivity ($D_{Li+}$) can be calculated using the following equation.

$$D_{Li}+ = \frac{4}{\pi\tau}\left(\frac{n_m V_m}{S}\right)^2\left(\frac{\Delta E_s}{\Delta E_t}\right)^2 \quad (14)$$

where, $\tau$ is the duration of the current pulse (s), $n_m$ is the number of moles (mol), $V_m$ is the molar volume of the electrode ($cm^3\ mol^{-1}$), S is the electrode/electrolyte contact area ($cm^2$), $\Delta E_s$ is the steady-state voltage change due to the current pulse, $\Delta E_t$ is the voltage change during the constant current pulse, eliminating the iR drop. The $D_{Li+}$ of $In_2O_3$/CNT_Ar was in the range of $2.84 \times 10^{-10}$ to $3.69 \times 10^{-12}$ $cm^2\ s^{-1}$ and $1.45 \times 10^{-10}$ to $6.76 \times 10^{-12}$ $cm^2\ s^{-1}$ for the discharge (Fig. S14b) and charge process (Fig. S14c), respectively. The $D_{Li+}$ of $In_2O_3$/CNT_Ar was higher than those of $In_2O_3$/CNT_Air and $In_2O_3$ regardless of the potential, indicating the superior lithium ion transport efficiency of $In_2O_3$/CNT_Ar, as consistent with the results from EIS analysis (Fig. 7**f**). Fig. 8 schematically illustrates the charge transport in $In_2O_3$/CNT_Ar during the charge-discharge process. Owing to the synergetic effects of the 0D $In_2O_3$-1D CNT structural characteristics and high oxygen vacancies, $In_2O_3$/CNT_Ar showed excellent electrochemical performance and kinetics compared to previously reported $In_2O_3$-based electrodes (Table S3).

Fig. 9 shows the full battery performance using $In_2O_3$/CNT_Ar as an anode and $LiNi_{0.6}Co_{0.2}Mn_{0.2}O_2$ (NCM622) as a cathode (NP ratio of 1:1.1). The $In_2O_3$/CNT_Ar||NCM622 full battery exhibited a reversible specific capacity of 120 mAh $g^{-1}$ at a current density of 100 mA $g^{-1}$ after 100 cycles, corresponding to the energy density of 348 Wh $kg^{-1}$. The obtained energy density is superior to those of full batteries recently reported (Table S4).

## 4. Conclusion

In this study, $In_2O_3$/CNT_Ar is proposed as a promising anode material for LIBs. $In_2O_3$/CNT_Ar was synthesized via solvothermal sol-gel synthesis followed by thermal annealing. Homogeneous distribution of $In_2O_3$ and CNT was achieved by using functionalized CNTs, selecting an appropriate dispersing solvent, and dissolving the $In_2O_3$ precursor in the CNT-dispersed solution, as confirmed by various analyses (SEM, TEM, and UV–vis spectroscopy). In addition, controlling the thermal

annealing conditions increased the number of oxygen vacancies in $In_2O_3$ and the surface area, which in turn increased the specific capacity, alleviated the volume change, and facilitated Li-ion diffusion during electrochemical reactions. CV and EIS measurements validated the enhanced kinetics of $In_2O_3$/CNT_Ar compared to those of its counterparts ($In_2O_3$/CNT_Air and $In_2O_3$). $In_2O_3$/CNT_Ar, with an optimized $In_2O_3$ to CNT ratio of 92:8 (w/w), demonstrated superior cycling performance compared to previous $In_2O_3$-based electrodes. It achieved a capacity of 830 mAh $g^{-1}$ at a current density of 200 mA $g^{-1}$ after 100 cycles, and 570 mAh $g^{-1}$ at 500 mA $g^{-1}$ after 200 cycles. Additionally, its rate capability was notable, maintaining 65% capacity retention at 5 A $g^{-1}$ compared to 100 mA $g^{-1}$. Therefore, this study presents a new composite electrode that can be utilized in next-generation LIBs.

## CRediT authorship contribution statement

**Minju Kim:** Writing – original draft, Validation, Investigation, Data curation. **Chanwoo Park:** Validation, Investigation, Data curation. **Wonjong Jung:** Writing – review & editing, Supervision, Methodology. **Jaehyun Hur:** Writing – review & editing, Validation, Supervision, Funding acquisition, Conceptualization.

## Declaration of Competing Interest

The authors declare that they have no known competing financial interests or personal relationships that could have appeared to influence the work reported in this paper.

## Data Availability

Data will be made available on request.

## Acknowledgments

This work was supported Korea Institute for Advancement of Technology (KIAT) grant funded by the Korea Government (MOTIE) (P0012451, The Competency Development Program for Industry Specialist), and the Basic Science Research Capacity Enhancement Project through a Korea Basic Science Institute (National Research Facilities and Equipment Center) grant funded by the Ministry of Education (2019R1A6C1010016). We thank the Smart Materials Research Center for IoT at Gachon University for its instrumental support (SEM measurement).

## Appendix A. Supporting information

Supplementary data associated with this article can be found in the online version at doi:10.1016/j.jallcom.2024.174796.

## References

[1] Y.E. Lim, W.S. Choi, J.H. Kim, Y.N. Ahn, I.T. Kim, The Sn–red P–Fe–based alloy materials for efficient Li–ion battery anodes, J. Ind. Eng. Chem. 121 (2023) 299–311.
[2] S. Kim, K. Park, Electrode design to mitigate the kinetic issue of cathodes in high energy lithium-ion batteries, J. Power Sources 547 (2022) 231916.
[3] H.G. Park, K. Min, K. Park, A synergistic effect of Na+ and Al3+ dual doping on electrochemical performance and structural stability of LiNi0. 88Co0. 08Mn0. 04O2 cathodes for Li-ion batteries, ACS Appl. Mater. Interfaces 14 (2022) 5168–5176.
[4] M.X. Tran, J.-Y. Woo, T.-A. Nguyen, S.-W. Lee, J.K. Lee, Thermolytically grafted silicon particles with ultrathin carbonaceous coating rich of phenyl moieties as lithium-storage anode material, Chem. Eng. J. 395 (2020) 125169.
[5] V.A. Tran, H.H. Do, T.D.C. Ha, S.H. Ahn, M.-G. Kim, S.Y. Kim, S.-W. Lee, Metal-organic framework for lithium and sodium-ion batteries: Progress and perspectivez, Fuel 319 (2022) 123856.
[6] U. Farva, H.W. Lee, R.-N. Kim, D.-G. Lee, D.-W. Kang, J. Kim, Growth temperature influence on atomic-layer-deposited In2O3 thin films and their application in inorganic perovskite solar cells, Nanomaterials 11 (2021) 2047.
[7] Q.Q.V. Thieu, W.G. Kidanu, H.D. Nguyen, T.L.T. Nguyen, M.L.P. Le, D.Q. Nguyen, N.T. Tran, X.V. Nguyen, I.T. Kim, T.L. Nguyen, Spinel Ni-ferrite advanced high-capacity anode for Li-ion batteries prepared via coprecipitation route, Ceram. Int. 48 (2022) 31470–31477.
[8] Q.H. Nguyen, V.D. Phung, W.G. Kidanu, Y.N. Ahn, T.L. Nguyen, I.T. Kim, Carbon-free Cu/SbxOy/Sb nanocomposites with yolk-shell and hollow structures as high-performance anodes for lithium-ion storage, J. Alloy. Compd. 878 (2021) 160447.
[9] J. Lee, W.S. Jung, S.-W. Lee, N-doped ZnC composites with gelatin coating as enhanced lithium-storage anode materials, J. Mater. Sci. 57 (2022) 21996–22005.
[10] C. Liang, M. Gao, H. Pan, Y. Liu, M. Yan, Lithium alloys and metal oxides as high-capacity anode materials for lithium-ion batteries, J. Alloy. Compd. 575 (2013) 246–256.
[11] D. Liu, X. Bai, J. Sun, D. Zhao, C. Hong, N. Jia, Hollow In2O3/In2S3 nanocolumn-assisted molecularly imprinted photoelectrochemical sensor for glutathione detection, Sens. Actuators B: Chem. 359 (2022) 131542.
[12] D.-W. Kim, I.-S. Hwang, S.J. Kwon, H.-Y. Kang, K.-S. Park, Y.-J. Choi, K.-J. Choi, J.-G. Park, Highly conductive coaxial SnO2− In2O3 heterostructured nanowires for Li ion battery electrodes, Nano Lett. 7 (2007) 3041–3045.
[13] S. Qin, D. Liu, W. Lei, Y. Chen, Synthesis of an indium oxide nanoparticle embedded graphene three-dimensional architecture for enhanced lithium-ion storage, J. Mater. Chem. A 3 (2015) 18238–18243.
[14] H. Zhao, H. Yin, X.-X. Yu, W. Zhang, C. Li, M.-Q. Zhu, In2O3 nanoparticles/carbon fiber hybrid mat as free-standing anode for lithium-ion batteries with enhanced electrochemical performance, J. Alloy. Compd. 735 (2018) 319–326.
[15] L. Yue, W. Zhang, W. Zhang, Q. Zhang, R. Guan, G. Hou, N. Xu, One-step solvothermal process of In2O3/C nanosheet composite with double phases as high-performance lithium-ion battery anode, Electrochim. Acta 160 (2015) 123–130.
[16] Y. Zhang, C. Jiang, S. Zhuang, M. Lu, Y. Cai, Mesoporous In 2 O 3 nanofibers assembled by ultrafine nanoparticles as a high capacity anode for Li-ion batteries, RSC Adv. 6 (2016) 49782–49786.
[17] J. Liu, Y. Zhu, J. Liang, Y. Qian, Synthesis of in2o3/carbon core-shell nanospheres and their electrochemical performance, Int. J. Electrochem. Sci. 7 (2012) 5574–5580.
[18] H. Yang, T. Song, S. Lee, H. Han, F. Xia, A. Devadoss, W. Sigmund, U. Paik, Tin indium oxide/graphene nanosheet nanocomposite as an anode material for lithium ion batteries with enhanced lithium storage capacity and rate capability, Electrochim. Acta 91 (2013) 275–281.
[19] C. De las Casas, W. Li, A review of application of carbon nanotubes for lithium ion battery anode material, J. Power Sources 208 (2012) 74–85.
[20] T.L. Nguyen, T.N. Vo, V.D. Phung, K. Ayalew, D. Chun, A.T. Luu, Q.H. Nguyen, K. J. Kim, I.T. Kim, J. Moon, Li-ion storage in orthorhombic hydrated sodium molybdate with oxygen-vacancy defects, Chem. Eng. J. 446 (2022) 137174.
[21] C.H. Lau, R. Cervini, S.R. Clarke, M.G. Markovic, J.G. Matisons, S.C. Hawkins, C. P. Huynh, G.P. Simon, The effect of functionalization on structure and electrical conductivity of multi-walled carbon nanotubes, J. Nanopart. Res. 10 (2008) 77–88.
[22] Y. Shimamura, K. Oshima, K. Tohgo, T. Fujii, K. Shirasu, G. Yamamoto, T. Hashida, K. Goto, T. Ogasawara, K. Naito, Tensile mechanical properties of carbon nanotube/epoxy composite fabricated by pultrusion of carbon nanotube spun yarn preform, Compos. Part A: Appl. Sci. Manuf. 62 (2014) 32–38.
[23] D. Rajendran, R. Ramalingame, A. Adiraju, H. Nouri, O. Kanoun, Role of solvent polarity on dispersion quality and stability of functionalized carbon nanotubes, J. Compos. Sci. 6 (2022) 26.
[24] T.T. Nguyen, S.U. Nguyen, D.T. Phuong, D.C. Nguyen, A.T. Mai, Dispersion of denatured carbon nanotubes by using a dimethylformamide solution, Adv. Nat. Sci. Nanosci. Nanotechnol. 2 (2011) 035015.
[25] J. Shi, X. Liu, F. Zhu, W. Tian, Y. Xia, T. Li, R. Rao, T. Zhang, L. Liu, Oxygen vacancy migration and its lattice structural origin in A-site non-stoichiometric bismuth sodium titanate perovskites, J. Mater. 8 (2022) 719–729.
[26] P. Li, C. Ruan, J. Xu, Y. Xie, Supercapacitive performance of CoMoO4 with oxygen vacancy porous nanosheet, Electrochim. Acta 330 (2020) 135334.
[27] G. Satish, V. Prasad, K. Ramji, Manufacturing and characterization of CNT based polymer composites, Math. Models Eng. 3 (2017) 89–97.
[28] Y. Zhao, J. Li, J. Xiang, R. Wu, C. Lyu, H. Ma, X. Song, J. Zhang, L. Wang, C. Zha, High electrochemical activity of Li2S2 linking two-dimensional tungsten boride nanosheet enables high-loading and long-lasting lithium-sulfur batteries, Mater. Today Energy 25 (2022) 100970.
[29] P.G. Collins, Defects and Disorder in Carbon Nanotubes, Oxford University Press, Oxford, 2010.
[30] S. Mallakpour, E. Khadem, Carbon nanotube–metal oxide nanocomposites: fabrication, properties and applications, Chem. Eng. J. 302 (2016) 344–367.
[31] C. Park, E. Samuel, B. Joshi, T. Kim, A. Aldalbahi, M. El-Newehy, W.Y. Yoon, S. S. Yoon, Supersonically sprayed Fe2O3/C/CNT composites for highly stable Li-ion battery anodes, Chem. Eng. J. 395 (2020) 125018.
[32] Y. Cheng, J. Huang, H. Qi, L. Cao, J. Yang, Q. Xi, X. Luo, K. Yanagisawa, J. Li, Adjusting the chemical bonding of SnO2@ CNT composite for enhanced conversion reaction kinetics, Small 13 (2017) 1700656.
[33] E. Flahaut, A. Peigney, C. Laurent, C. Marliere, F. Chastel, A. Rousset, Carbon nanotube–metal–oxide nanocomposites: microstructure, electrical conductivity and mechanical properties, Acta Mater. 48 (2000) 3803–3812.
[34] J. Gan, X. Lu, J. Wu, S. Xie, T. Zhai, M. Yu, Z. Zhang, Y. Mao, S.C.I. Wang, Y. Shen, Oxygen vacancies promoting photoelectrochemical performance of In2O3 nanocubes, Sci. Rep. 3 (2013) 1021.
[35] A. Nasriddinov, T. Shatalova, S. Maksimov, X. Li, M. Rumyantseva, Humidity effect on low-temperature NH3 sensing behavior of In2O3/rGO composites under UV activation, Sensors 23 (2023) 1517.

[36] S. Kim, T. Park, H.J. Yun, H. Yoo, Observation of controllable negative differential resistance behaviors through morphology-dependent zinc oxide/p-Si heterointerface structures, Adv. Mater. Technol. 7 (2022) 2201028.
[37] T. Munawar, F. Iqbal, S. Yasmeen, K. Mahmood, A. Hussain, Multi metal oxide NiO-CdO-ZnO nanocomposite–synthesis, structural, optical, electrical properties and enhanced sunlight driven photocatalytic activity, Ceram. Int. 46 (2020) 2421–2437.
[38] F. Gu, C. Li, D. Han, Z. Wang, Manipulating the defect structure (VO) of In2O3 nanoparticles for enhancement of formaldehyde detection, ACS Appl. Mater. Interfaces 10 (2018) 933–942.
[39] B. Xiao, F. Wang, C. Zhai, P. Wang, C. Xiao, M. Zhang, Facile synthesis of In2O3 nanoparticles for sensing properties at low detection temperature, Sens. Actuators B: Chem. 235 (2016) 251–257.
[40] L. Gao, Z. Cheng, Q. Xiang, Y. Zhang, J. Xu, Porous corundum-type In2O3 nanosheets: synthesis and NO2 sensing properties, Sens. Actuators B: Chem. 208 (2015) 436–443.
[41] W.J. Kim, D. Pradhan, Y. Sohn, Fundamental nature and CO oxidation activities of indium oxide nanostructures: 1D-wires, 2D-plates, and 3D-cubes and donuts, J. Mater. Chem. A 1 (2013) 10193–10202.
[42] Y. Huang, K. Yu, Z. Zhu, Controllable synthesis of novel In2O3 nanostructures and their field emission properties, Cryst. Res. Technol. 46 (2011) 90–94.
[43] H. Xu, L. Wang, J. Zhong, T. Wang, J. Cao, Y. Wang, X. Li, H. Fei, J. Zhu, X. Duan, Ultra-stable and high-rate lithium ion batteries based on metal–organic framework-derived In2O3 nanocrystals/hierarchically porous nitrogen-doped carbon anode, Energy Environ. Mater. 3 (2020) 177–185.
[44] W.-H. Ho, C.-F. Li, H.-C. Liu, S.-K. Yen, Electrochemical performance of In2O3 thin film electrode in lithium cell, J. Power Sources 175 (2008) 897–902.
[45] Y.M. Chen, L. Yu, X.W. Lou, Hierarchical tubular structures composed of Co3O4 hollow nanoparticles and carbon nanotubes for lithium storage, Angew. Chem. Int. Ed. 55 (2016) 5990–5993.
[46] C. Hou, Y. Hou, Y. Fan, Y. Zhai, Y. Wang, Z. Sun, R. Fan, F. Dang, J. Wang, Oxygen vacancy derived local build-in electric field in mesoporous hollow Co 3 O 4 microspheres promotes high-performance Li-ion batteries, J. Mater. Chem. A 6 (2018) 6967–6976.
[47] F. Wu, J. Bai, J. Feng, S. Xiong, Porous mixed metal oxides: design, formation mechanism, and application in lithium-ion batteries, Nanoscale 7 (2015) 17211–17230.
[48] T.T. Salunkhe, A.N. Kadam, J. Hur, I.T. Kim, Green and sustainably designed intercalation-type anodes for emerging lithium dual-ion batteries with high energy density, J. Energy Chem. 80 (2023) 466–478.
[49] Y. Wang, T. Zhou, K. Jiang, P. Da, Z. Peng, J. Tang, B. Kong, W.B. Cai, Z. Yang, G. Zheng, Reduced mesoporous Co3O4 nanowires as efficient water oxidation electrocatalysts and supercapacitor electrodes, Adv. Energy Mater. 4 (2014) 1400696.
[50] E. Park, S. So, J. Hur, Carbon-free hydrated cobalt vanadium oxide as a promising anode for lithium-ion batteries, Appl. Surf. Sci. 579 (2022) 152182.
[51] G. Lee, I.T. Kim, J. Hur, Highly conductive and robust telluride-carbon hybrid matrix for enhanced copper diphosphide anode in Li-ion batteries, J. Alloy. Compd. 950 (2023) 169914.
[52] J. Ko, M. Kim, S. So, I.T. Kim, J. Hur, Electron-rich hybrid matrix to enhance molybdenum oxide-based anode performance for Lithium-Ion batteries, J. Colloid Interface Sci. 647 (2023) 93–103.
[53] X. Liu, R. Wang, S. Liu, J. Pu, H. Xie, M. Wu, D. Liu, Y. Li, J. Liu, Organic eutectic salts-assisted direct lithium regeneration for extremely low state of health Ni-rich cathodes, Adv. Energy Mater. 13 (2023) 2302987.
[54] F. Zhou, R. Wang, S. He, X. Liu, S. Liu, H. Shao, X. Liu, Z. Xiao, J. Liu, Defect-rich hierarchical porous Mn-doped CoP hollow microspheres accelerate polysulfide conversion, Adv. Funct. Mater. 33 (2023) 2211124.